J Mater Sci (2007) 42:1584–1593
DOI 10.1007/s10853-006-0696-1

NANOSTRUCTURED MATERIALS-PROCESSING, STRUCTURES, PROPERTIES AND APPLICATIONS

Characterization of nanocrystalline materials by X-ray line profile analysis

Tamás Ungár

Received: 31 May 2006 / Accepted: 20 July 2006 / / Published online: 21 December 2006

Abstract X-ray line profile analysis is shown to be a powerful tool to characterize the microstructure of nanocrystalline materials in terms of grain and subgrain size, dislocation structure and dislocation densities and planar defects, especially stacking faults and twin boundaries. It is shown that the X-ray method can provide valuable complementary information about the microstructure, especially when combined with transmission electron microscopy and differential scanning calorimetry.

Introduction

The characterization of nanostructured solids or nanocrystalline materials comprises the description of microstructure in terms of (i) grain size and (ii) lattice defects. Grain size, in general, is routinely determined by analyzing transmission electron microscopy (TEM) micrographs. Looking more carefully at TEM micrographs reveals, however, that grain size is often more subtle than just the obvious boundary contours, cf. [1]. The orientation differences on the adjacent sides of the grain boundary contrasts can vary between almost zero and any other value. Overlapping grains within the thin foil, especially in the case of the smallest grain size regime, can produce apparent additional contrasts. On the other hand, faint contrasts, especially when the orientation differences are small, can escape grain boundary counting. Still, TEM micrographs are unavoidable for grain size determination. An alternative tool to determine grain size, particularly in the submicron regime, is X-ray line broadening. It is being used ever since the pioneering work of Scherrer in 1918 [2], who realized that the optical principles of X-ray scattering are not so far from the principles of light scattering. The shrinkage of a grating causes spreading of diffraction spots, which we have all seen with naked eyes during our basic physics courses. Today, with all the sophisticated X-ray sources, diffractometers, detectors and theories, we can do a lot more. Warren [3–5], Wilson [6] and Bertaut [7] have started the art of X-ray line profile analysis in the forties and fifties by showing that lattice strain has considerable contribution to line broadening and, if this is given due care, far more can be derived about size and size-distribution than just the Scherrer equation. Strain is frequently given as a number related to the root-mean-square strain, $<\varepsilon^2>^{1/2}$, which is, on the one hand an unnecessary simplification, on the other hand, physically incorrect, since the root-mean-square strain is a strongly distance dependent, at short distances singular quantity, cf. [8]. The sources of strain can be (i) dislocations, (ii) grain boundary triple junctions, (iii) contact or sinter stresses, (iv) stacking faults, (v) coherency stresses, and others, most of which can be physically well modeled and derived explicitly from line profile analysis. X-ray line profile analysis is, in general, an averaging method. The illuminated volume is usually many orders of magnitude larger than the volume probed by a TEM micrograph. This feature gives an excellent opportunity to gain different and complementary information by using both, the X-ray and

---

T. Ungár (✉)
Department of Materials Physics, Eötvös University
Budapest, Budapest, Hungary
e-mail: ungar@ludens.elte.hu

TEM methods to describe microstructure. In the present account the fundamental information provided by the X-ray method is reviewed, and where possible, the correlation with TEM observations is pointed out.

Fundamentals of X-ray line profile analysis

X-ray diffraction patterns of nanostructured solids or nanocrystalline materials consist of broadened diffraction peaks. In the present context, information about crystal structure and phase analysis are not considered. Broadening is caused by smallness of crystallites and strain. By the kinematical theory of scattering the measured physical profile, $I^F_{hkl}$of the *hkl* Bragg reflection can be given as the convolution of the size and strain profiles, $I^S_{hkl}$and I^D_{hkl}, respectively [5]:

$$I^F_{hkl} = I^S_{hkl} * I^D_{hkl} \tag{1}$$

If stacking faults or twinning are significant lattice defect in the material, the equation can be extended by the profiles corresponding to stacking faults or twin boundaries, I^{SF}_{hkl} [9]:

$$I^F_{hkl} = I^S_{hkl} * I^D_{hkl} * I^{SF}_{hkl} \tag{2}$$

The detailed expressions of the three different profile functions, I^S_{hkl}, I^D_{hkl} and I^{SF}_{hkl}, were derived and modeled in different ways in the various methods and procedures of line profile analysis. In the following these are surveyed with special reference to nanocrystalline materials.

Grain size, subgrain size

The size profile is the sum of the intensities diffracted by parallel and independent columns aligned normal to the reflecting planes with unit cross sectional area. The diffraction peak corresponding to a particular column is the squared Fourier transform of the form-factor of that column in the direction parallel to the diffraction vector [7]. The size profile, I^S_{hkl}will be the volume-weighted sum of the individual peaks corresponding to the individual columns. Its physical meaning is related to the area or volume weighted column-length distribution in the specimen, where the two different weightings are directly connected to the Fourier transforms or the integral breadths of the size profile, respectively [7]. Krill and Birringer [10] have shown that the two weightings can also be directly related to two different momentums of the Fourier transforms of I^S_{hkl}. The column-length distribution in the specimen depends on the size, the shape and the size distribution of the crystallites. It has to be noted, however, that different crystallite shapes and size-distributions can have the same column-length distribution, which means that the correlation between column-length distribution and crystallite shapes and size-distributions is not unique. Therefore, in order to obtain the mean size of crystallites and/or their size-distributions, assumptions have to be made about the shape and the specific functional form of size-distribution, cf. [11–13]. Here we note that for testing assumptions about size distribution functions Langford and coworkers [13] have studied the size and size-distribution in loose nanopowders with minimal strain, especially in ball milled and compacted ceria powders. The log-normal size distribution function, $f(x)$, given by the median m and the variance σ, has been shown to describe size-distribution in a wide range of bulk or loose powder materials, cf. [10–16]. Hinds [17] has shown that the arithmetic-, the area- and the volume-weighted mean crystallite diameters can be given with m and σ:

$$<x>_j = m\exp(k\sigma^2) \tag{3}$$

where j means arithmetic-, area- or volume-weighting and k = 0.5, 2.5 and 3.5 for the different averaging, respectively. The explicit form of the size profile, I^S_{hkl}or its Fourier transform, as it is used in the multiple whole profile (MWP) or convolutional multiple whole profile (CMWP) fitting procedures, can be found in [18–20].

One of the first concomitant determination of the size distribution function by TEM and X-ray line profile analysis was done by Krill and Birringer on ball milled and compacted nanocrystalline palladium [10]. The size Fourier coefficients were determined by the Warren–Averbach method using the {111} and {222} reflections. It was shown that the intercept of the initial slope and the integral of the size Fourier coefficients give the area and volume weighted mean crystallite size, respectively, and from these two mean values the median and the variance of the log normal size distribution function were evaluated. Figure 1 shows a good correlation between the TEM counting and the log normal size distribution function determined from X-ray diffraction. In ball milled and subsequently sintered Tungsten–Carbide the size distribution of crystallites was determined by TEM counting and X-ray diffraction [12]. The good correlation between the two size distributions is shown in Fig. 2. Here the median and the variance of the log normal size distribution function were evaluated from the full width at half maximum (FWHM), the integral breadths

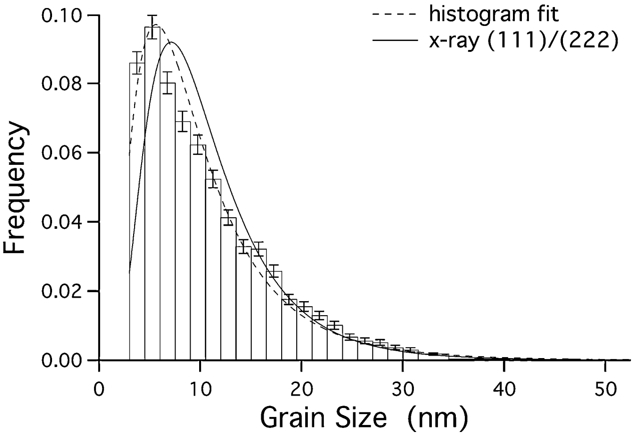

Fig. 1 Correlation between the TEM counting (histogram and dashed line) and the log normal size distribution function (solid line) determined from X-ray diffraction for inert gas condensed and conpacted Pd. The X-ray size distribution was determined by analysing the size Fourier coefficients of the profiles of the {111} and {222} Bragg reflections. (By courtecy of Professor C. E. Krill, see also ref. [10])

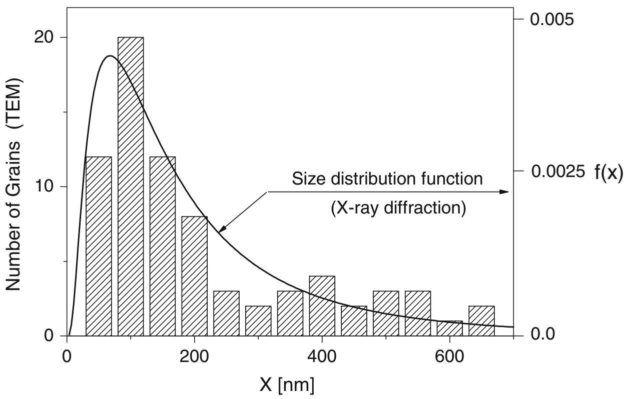

Fig. 2 Correlation between the TEM counting (histogram) and the log normal size distribution function (solid line) determined from X-ray diffraction for ball milled and sintered WC. The X-ray size distribution was obtained by using the *modified* Williamson-Hall and *modified* Warren-Averbach methods [12, 21]

and the size Fourier coefficients of all measured Bragg reflections, where strain anisotropy was taken care of by the dislocation contrast factors, cf. [21, 22]. The more reliable and robust method of whole profile fitting procedure, MWP [17, 18] was applied to determine the size distribution in inert gas condensed and subsequently compacted nanocrystalline copper [23–25]. Figure 3 shows typical log normal size distribution functions obtained by TEM counting and X-ray diffraction, respectively. Both, the TEM and the X-ray data suggest, in good correlation with each other, that nanocrystalline copper may reveal spontaneous grain growth at room temperature, well below temperatures of recovery or recrystallisation.

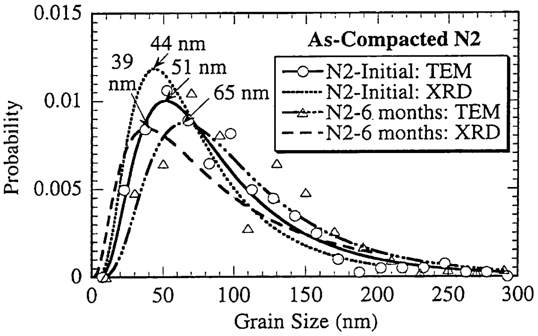

Fig. 3 Size distribution of nanocrystalline grains in inert gas condensed and subsequently compacted nanocrystalline copper determined by TEM counting (open circles with solid line, and open triangles with dash-dotted line) and X-ray diffraction (dotted, and dashed lines), respectively [23–25]. The X-ray size distribution was assumed to be log-normal

In the case of nanostructured materials produced by different modes of severe plastic deformation (SPD), e.g. equal channel angular pressing (ECAP), high pressure torsion (HPT) or ball milling and subsequent compaction, the grain size determined by TEM counting or X-ray diffraction reveal an apparent discrepancy. Usually, TEM counting provides a larger average grain size than X-ray diffraction. Figure 4 shows a comparison of the average grain size determined by TEM counting, $<d>_{\mathrm{TEM}}$, versus the area average mean crystallite size given by X-ray diffraction, $<x>_{\mathrm{area,\ X\text{-}ray}}$ (for the data in the figure see [14, 19, 23–30]). The figure shows that, in the case of the copper specimens prepared by inert gas condensation and compaction and a few specimens prepared by SPD methods, especially in the smallest grain size regime, there is a good correlation between TEM counting and X-ray diffraction. The one-to-one correlation is indicated by the dash-dotted line of unit slope. However, in the case of most of the specimens prepared by SPD methods the TEM counting gives larger average grain size than X-ray diffraction. This is even true in the smaller grain size regime, as shown in Fig. 4b. The dashed line in Fig. 4a is only for the purpose of guiding the eye. The reason for this apparent discrepancy is that the size provided by X-ray diffraction corresponds to the average of the smallest undistorted regions in the material, whereas TEM counting is related to regions separated by more-or-less sharp contours in the TEM micrograph. One possible explanation for the discrepancy would be that when dislocations are arranged in a configuration which causes small orientation differences between two adjacent regions, the X-ray size corresponds to the two separate regions, whereas in the TEM micrograph the two regions may seem to correspond to the same grain, therefore the boundary

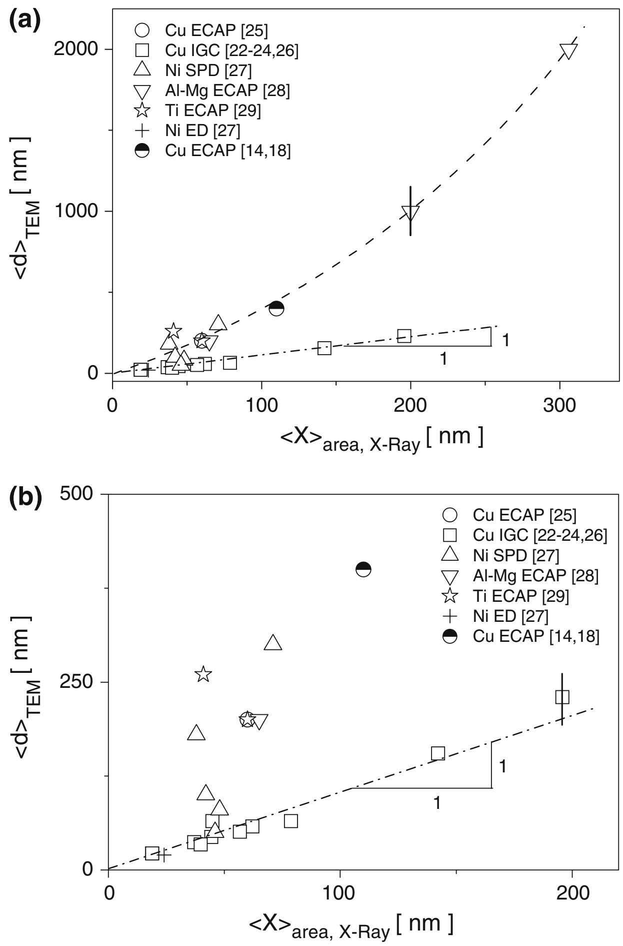

Fig. 4 Average grain size determined by TEM, $\langle d\rangle_{\mathrm{TEM}}$, versus the area average mean crystallite size, $\langle x\rangle_{\mathrm{area,\ X\text{-}Ray}}$, determined by X-ray analysis for ECAP deformed Cu (open circles [26]), inert gas condensed and compacted Cu (open square [23–25,27]), severe plastic deformed Ni (open up-triangle [28]), ECAP deformed Al-Mg (open down-triangle [29]), ECAP deformed Ti (open star [29]), electrodeposited Ni (cross [28]), and ECAP deformed Cu (half full circle [14,19]). Figure (b) is the blown up lower-left corner region of figure (a). The vertical line in figure (a) indicate the experimental errors

between them is not taken as grain boundary, cf [31]. These dislocation configuration can be considered as small-angle grain-boundary (SAGB) configurations. The corresponding smallest regions are subgrains separated by subboundaries of SAGB type. Hellmig and coworkers [1] have systematically investigated the grain and subgrain size distribution and the orientation conditions between them in copper specimens deformed by ECAP. They found that there are distinctly different grain size distributions which can be classified according to the orientation differences between adjacent grains or subgrains. Especially, it was found that there is a considerable volume fraction of subgrains separated by subboundaries on the two sides of which the orientation differences are close to zero. Encouraged by this finding the effect of subboundaries with dipolar dislocation configuration was investigated in [32]. It was shown that when a subboundary consists of a dipolar dislocation-wall (DiDW) the lattice planes on either side of such a wall are shifted toward each other, where this shift varies randomly from subgrain to subgrain, between zero and b/2, where b is the Burgers vector. This spatially random shift causes a random phase shift of the X-rays scattered by the adjacent subgrains. This means that subgrains separated by subboundaries of DiDW type are also coherently scattering domains, just as the subgrains separated by SAGB type subboundaries. The two models, i.e. the SAGB and the DiDW model of subgrain boundaries, provide together a physically well established basis for the assumption that size and size-distributions determined by X-ray diffraction correspond to subgrains or dislocation cells. Obviously, if the subgrains or the dislocation cells and the grains are identical, then the TEM and X-ray size data can be identical. This happens in the case of the inert gas condensed and compacted copper specimens in which there are no subgrains but just grains separated mainly by large angle grain boundaries. It has to be noted here that in a real material neither the SAGB type nor the DiDW type subboundaries will be perfectly of one type. There may be some dislocation dipoles in the SAGBs or uncompensated excess dislocations in a DiDW type subboundaries. Real subboundaries will probably be once closer to SAGB or in other cases closer to DiDW type.

Microstrains and dislocations

Microstrains are one of the major source of lattice distortion in nanostructured materials. They are caused by (i) dislocations, (ii) triple junctions of grain or subgrain boundaries, (iii) contact or sinter stresses, and (iv) to some extent by planar defects, especially stacking faults and twin boundaries. The strain fields of dislocations, triple junctions and contact stresses are usually heterogeneous and of long range character, i.e. the deformation decays as the reciprocal distance, cf. [8, 33, 34]. Basically they cause X-ray line broadening without line shift, where the broadening increases with diffraction order, cf. [5]. The increase is, however, not monotonous, but it varies with *hkl* in a strict correlation with the (a) elastic anisotropy of the materials, cf. [33, 35–38] and (b) the specific types and species of lattice defects, cf. [18], and the phenomenon is called strain anisotropy [39]. Since the spatial dependence of the deformation corresponding to the three major types of lattice defects, i.e. dislocations, triple junctions and contact stresses, is not distinctly different, one has to satisfy with the analysis of dislocations as one of the prototypes of the source of microstrain. It can be shown that other sources of microstresses can be quantified in terms of dislocation properties, cf. [40]. The Fourier transform of the strain profile, I^D_{hkl}, can be best given by the Wilkens function, $f(\eta)$ [8]:

$$\begin{aligned} A^D_{hkl} &= \exp\left[-2\pi^2 L^2 g^2 < \varepsilon^2_{g,L} >\right] \\ &= \exp\left[-2\pi^2 L^2 g^2 (b/2\pi)^2 \pi\rho C f(\eta)\right] \end{aligned} \tag{4}$$

where $<\varepsilon^2_{\mathbf{g},L}>$ is the mean square strain, mentioned before, L is the Fourier variable, a distance in the crystal, g is the absolute value of the diffraction vector $\mathbf{g}$, b is the absolute value of the Burgers vector of dislocations, ρ is the dislocation density, C is the contrast (or orientation) factor of dislocations, $\eta = L/R_e$, R_e is the effective outer cut-off radius of dislocations and $<\varepsilon^2_{g,L}> = (b/2\pi)^2\pi\rho C f(\eta)$. The specific value of R_e can only be interpreted physically together with the value of ρ. For this purpose Wilkens introduced the dimensionless quantity $M = R_e\sqrt{\rho}$ [8, 41]. The value of M is smaller or larger than unity as (i) the profile tails are longer or shorter, (ii) as the average exponent in the ΔK dependence of the asymptotic behavior of the tails of profiles is closer to –3 or –2, (iii) as the screening of strain fields of dislocations is stronger or weaker and (iv) as the dipole character of dislocations is stronger or weaker, respectively. All formulations in (i) to (iv) have the same physical meaning.

Strain anisotropy

The non-monotonous variation of X-ray line broadening with *hkl* was observed by Stokes and Wilson in the nineteen forties [42]. In powder diffraction crystallography it is known as strain anisotropy [39]. It means that neither the breadths nor the Fourier coefficients of diffraction profiles are monotonous functions of the diffraction angle or g. Several authors have shown that as long as crystal defects, especially dislocations, do not break the crystal symmetry, strain anisotropy can be scaled in terms of the elastic anisotropy of the crystal, i.e. either in terms of the anisotropic elastic constants, E_{hkl}, cf. [38, 43] or in terms of the fourth order invariants of the *hkl* indices, cf. [33, 42]. It can be shown that the two representations are equivalent [44, 45]. Crystal defects, in particular dislocations, do not break the crystal symmetry as long as the Burgers vectors and the slip systems are randomly populated, i.e. as long as their strain field can be averaged over the permutations of the *hkl* indices. It was shown that in these particular cases the contrast (or orientation) factors of dislocations, $C(hkl,c_{ijkl})$ (where c_{ijkl} are the elastic constants of the crystal), can be averaged over the permutations of the *hkl* indices, and that the average dislocation contrast factors, $\overline{C}$, will be linear functions of the fourth order invariants of the *hkl* indices [22]. In particular, for cubic and hexagonal crystals the average dislocation contrast factors are [22, 46]:

$$\overline{C} = \overline{C}_{h00}(1 - qH^2), \tag{5}$$

and

$$\overline{C}_{hk.l} = \overline{C}_{hk.0}\,[1 + q_1 x + q_2 x^2], \tag{6}$$

respectively, where $\overline{C}_{h00}$ is the average dislocation contrast factor of the *h00* type reflections and $H^2 = (h^2k^2 + h^2l^2 + k^2l^2)/(h^2 + k^2 + l^2)^2$. The values of $\overline{C}_{h00}$ and the q parameter can be obtained numerically for different dislocation types as functions of the elastic properties of a crystal [47]. In (6) $\overline{C}_{hk.0}$ is the average dislocation contrast factor of the *hk.0* type reflections, $x = (2/3)(l/ga)^2$, where a is the lattice constant in the basal plane, and q_1 and q_2 are numerical constants depending on the Burgers vector type and elastic constants of the crystal. The values of $\overline{C}_{h00}$, q, and $\overline{C}_{hk.0}$, q_1 and q_2 are compiled in [47, 48] and [46], respectively. In [47, 48] it was shown that the q parameter is different for different Burgers vector types, and for edge or screw dislocations in cubic crystals. The typical behavior of the q parameter in *fcc* crystals for the *a*/2 <110>{111} slip system as a function of the Zener constant, $A_Z = 2c_{44}/(c_{11}–c_{12})$, is shown in Fig. 5. It can be seen that the q parameter values are very different for edge or screw dislocations. It is also found that in the case of screws they are independent, and for edges they slightly depend of the c_{12}/c_{44} ratio, as indicated in the figure. The solid lines are polynomial curves fitted to the numerically calculated values shown as open symbols. In [46] it was shown that the q_1 and q_2 parameters are different for different slip systems in hexagonal crystals. The variation of the q, and q_1 and q_2 parameters with different Burgers vector and slip system types can be considered as a weak violation of crystal symmetry. This means that the linearity of the average dislocation contrast factors with the fourth order invariants of the *hkl* indices is still maintained, but the coefficients in the linear function

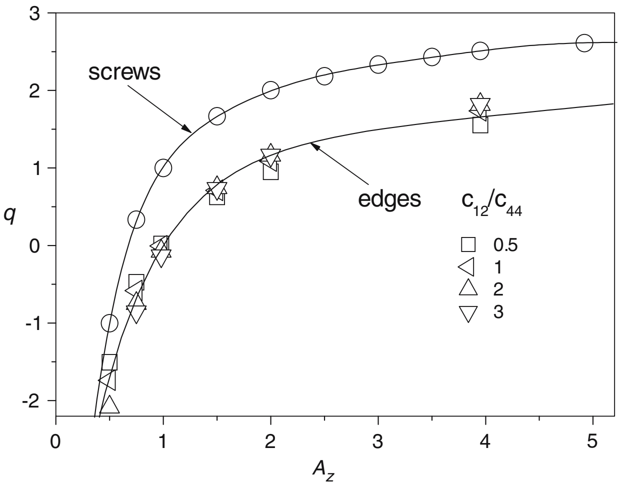

Fig. 5 Numerically calculated, theoretical values of the q parameter for fcc crystals for screw and edge dislocations, respectively. The q parameter is defined in eq. (5), and $A_Z = 2c_{44}/(c_{11}-c_{12})$ is the elastic anisotropy, where c_{ij} are the elastic constants of the crystal. For screw dislocations there is no dependence of q on c_{12}/c_{44}, in the case of edges there is a weak dependence, cf [46, 47]

vary with the Burgers vector and slip system types. A strong violation of crystal symmetry can be observed if single crystals or single grains with specific dislocations are analyzed by X-ray diffraction, cf. [49, 50]. The discussion of this effect is out of the frame of the present account.

Application to specific nanostructured materials

The potentials of X-ray line profile analysis in characterizing nanostructured materials is shown by the example of ball milled Al and two Al–Mg alloys [20]. High-purity Al powder and 3 and 6 wt.% high-purity Mg chips were mechanically alloyed in a Spex8000 shaker miller at room temperature for 3 h [51]. X-ray diffraction patterns were measured in a Philips X'pert powder diffractometer using CuKα radiation and secondary graphite monochromator. In order to have good counting statistics the data collection was carried for 30 h at 40 kV and 30 mA X-ray tube power. The instrumental pattern was obtained by a NIST SRM660a LaB6 peak profile standard material. The measured diffraction pattern corresponding to the Al-3 wt%Mg alloy after 3 h milling period is shown in Fig. 6 by open circles. The evaluation was carried out by the CMWP procedure for the dislocation density and arrangement parameters, ρ and M, the median and the variance in the log-normal size distribution function, m and σ, and the q parameter for strain anisotropy. The theoretical pattern, which is the convolution of the size and strain profiles and the measured instrumental pattern plus the background intensity, is shown in Fig. 6 as a solid line. Note the logarithmic intensity scale which enables to see the intensity distribution also in the lower intensity regions. The physical parameters provided by the CMWP procedure are shown in Fig. 7. In Fig. 7a it can be seen that the stored dislocation density increases by about a factor of ten as the Mg content increases to 6 wt%. Concomitantly the average subgrain size and the value of m are decreasing by a factor of three. Figure 7b shows that the values of M decreases, whereas that of q increases with Mg content. The log-normal size distribution functions in the pure Al and the Al-6 wt%Mg specimen are shown in Fig. 7c. The size distributions and the m and $\langle x\rangle_{\text{area}}$ values in Fig. 7a are in good correlation. The data can be summarized as follows. With increasing Mg content more dislocations are stored, probably because dynamical recovery is strongly hindered by solute Mg. Here we note that after 3 h ball milling the entire 6 wt% Mg was found to be in solid solution [51]. For the same reason, dynamic grain growth during ball milling is hampered with increasing Mg. The Zener constant of Al is $A_Z \cong 1.3(\pm0.04)$. With this value, from Fig. 5 it can be seen that for edge and screw dislocations $q = 0.6(\pm0.05)$ and $q = 1.6(\pm0.05)$, respectively. The measured values decrease with Mg content form about $q = 1.3(\pm0.2)$–$q = 0.7(\pm0.2)$. This means that in pure Al and the Al-3 wt%Mg alloys the dislocation character is average between edge and screw, or perhaps, somewhat closer to screw character. In the Al-6 wt%Mg alloy, however, edge dislocation character is

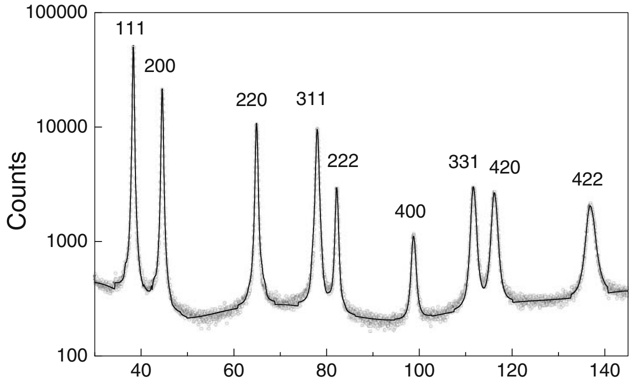

Fig. 6 The mesured (open circles) and fitted (solid line) diffraction pattern corresponding to the Al-3 wt%Mg alloy after 3 h milling period, cf [20]. Only each 5th measured point (open circle) is shown in the figure. Note the logarithmic intensity scale in order to have a better view in the lower intensity region. For the same reson no difference curves can be plotted

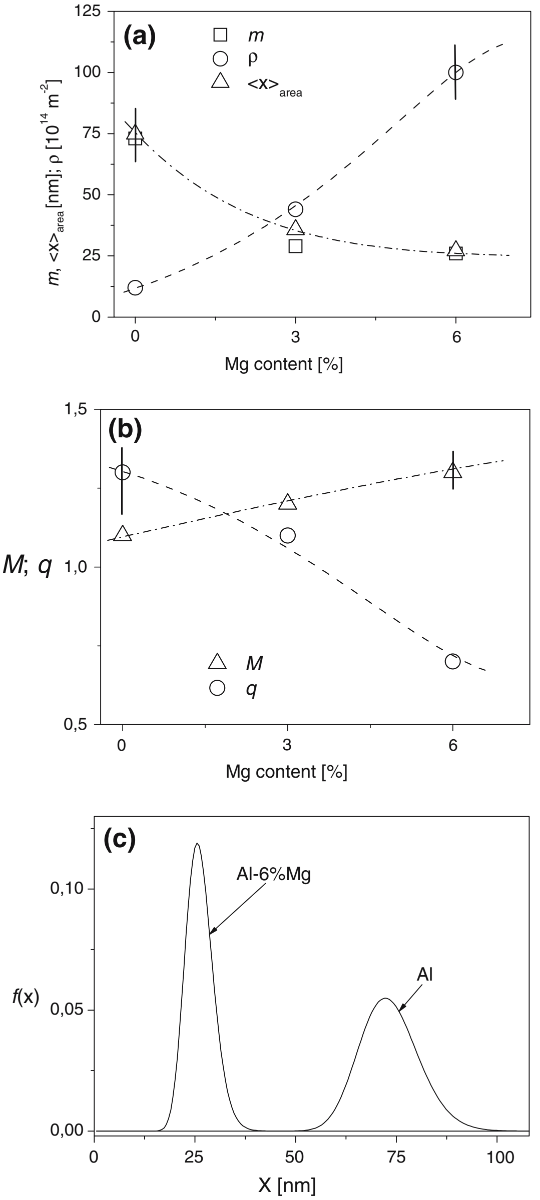

Fig. 7 (a) The median of the log normal size distribution, m (open square), the dislocation density, ρ (open circle) and the area average mean crystallite size, $<x>_{\text{area}}$ (open triangle) as a function of Mg content after ball milling. (b) The dislocation arrangement parameter, M (open circle) and the q parameter (open triangle) as a function of Mg content after ball milling. (c) The log-normal size distribution functions of crystallites in Al and in the Al-6%Mg alloy after 3 h ball milling. The vertical lines in figures (a) and (b) indicate the experimental errors

dominating. This latter is in good correlation with the extremely high dislocation density, $\rho \cong 10^{16}$ m^{-2}, where the annihilation of screw dislocations is more likely. The increase of the M parameter indicates that the dislocation arrangement is becoming more random with increasing Mg content. These results are in correlation with TEM observations in Al and Al–Mg alloys deformed by the method of ECAP [29].

The thermal stability of the microstructure was followed by combining X-ray line profile analysis and differential scanning calorimetric (DSC) investigations in Al alloys [52], and pure copper [26, 53] and titanium [54] deformed by HPT or ECAP, respectively. Figure 8 shows the heat flow, the dislocation density, ρ, and the area average mean crystallite size as a function of annealing temperature in an Al–Mg–Sc–Zr alloy deformed by 15 rotations in HPT [52]. The heat flow was measured in the scanning mode, whereas the other two parameters were measured after 10 min annealing at each indicated temperature. It can be seen that the dislocation density annihilates almost completely while the crystallite size is still unchanged at 450 K (177 °C), indicating that the disappearance of dislocations precedes grain growth in this alloy. The thermal stability of the microstructure in Cu deformed by 8 ECAP passes is shown in Fig. 9 [26, 53]. The dislocation density decreases gradually and drops to $\rho = 5 \times 10^{13}$ m^{-2} at 530 K (257 °C). Here the decrease of ρ and the increase of $<x>_{\text{area}}$ occur together. At the $T = 510$ K (237 °C), indicated by the vertical arrow, abnormal grain growth produces a bimodal grain structure with regions completely recrystallized, and embedded in regions with the original nanostructure. This is the bimodal structure reported by Ma and coworkers [55] and Kuzel and coworkers [56]. In this state of the material the diffraction peaks are the sum of two peaks with very different widths, see Fig. 4 in [26], which were not evaluated quantitatively. Figure 10 shows the heat flow, the dislocation density,

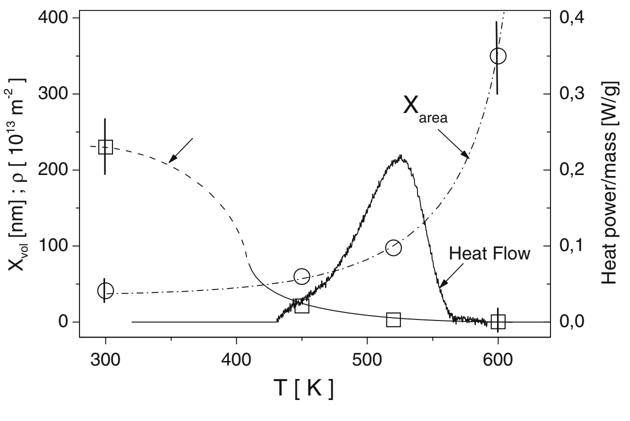

Fig. 8 The heat flow, the dislocation density, ρ (open squares), and the area average mean crystallite size, $<x>_{\text{area}}$ (open circles), as a function of annealing temperature in an Al–Mg–Sc–Zr alloy deformed by 15 rotations in HPT [52]. The dashed or solid lines through the discrete data points are to guide the eye. The vertical lines indicate the experimental errors

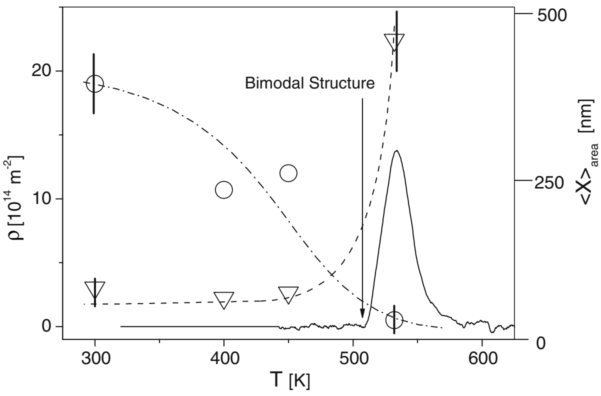

Fig. 9 The heat flow, the dislocation density, ρ (open circles), and the area average mean crystallite size, $<x>_{area}$ (open down-triangles), as a function of annealing temperature in Cu deformed by eigth ECAP passes [26, 53]. The dashed or dash-dotted lines through the discrete data points are to guide the eye. The vertical arrow indicates the temperature where the bimodal size distribution structure is formed. The vertical lines indicate the experimental errors

ρ, and the volume average mean crystallite size, $<x>_{vol}$, in Ti deformed by eight ECAP passes at 400–450 °C in the B_c mode, as a function of temperature [54]. It can be seen that the dislocation density decreases gradually with temperature until it reaches a value of about $\rho = 5 \times 10^{13}$ m^{-2} at the recrystallization temperature. However, the average crystallite size remains almost constant up to about 800 K (527 °C), indicating that in Ti grain growth starts at higher temperatures than dislocation annihilation.

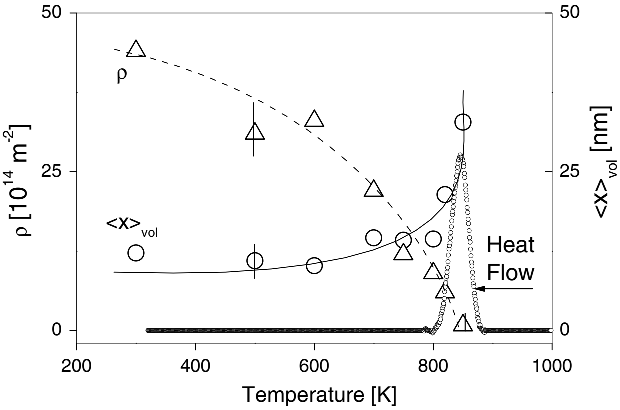

Fig. 10 The heat flow (small open circles), the dislocation density, ρ (open triangles), and the volume average mean crystallite size, $<x>_{vol}$ (open circles), as a function of annealing temperature in T_i deformed by eight ECAP passes at 400–450 °C in the B_c mode [54]. The dashed or solid lines through the discrete data points are to guide the eye. The vertical lines indicate the experimental errors

Stacking faults and twin boundaries

Twinning has been observed to be an alternative mechanism of plastic deformation in even high stacking fault materials as Al or Cu when the grain size becomes small enough, cf. [23–25, 27, 57–59]. The effect of stacking faults and twinning was first treated by Warren in the 1950s [5]. Using the method of series expansions and approximations Warren has shown that stacking faults or twin boundaries can be incorporated into the Fourier method of line profile analysis by introducing an apparent particle size which is a reduced version of the true particle size, where the reduction is caused by the planar defects. Warren calculated *hkl* dependent numerical factors. The *hkl* dependent reduction of the true particle size can be given by these numerical factors proportional to the density of planar defects. Warren's other result is still more relevant to the effect of planar defects. Describing the *fcc* crystal system by hexagonal coordinates, where l is perpendicular to the close packed planes, Warren has shown that there are two groups of *hkl* indices for which the planar faults affect the diffraction profiles in different ways: (i) if $h–k = 3$m, the planar faults do not effect line profiles, where m is an arbitrary integer, and (ii) if $h–k \neq 3$m the planar faults cause line broadening and shifts. The conditions of Warren in the hexagonal system can be reformulated in the cubic system as: (i) if $h + k + l = 3$m the planar defects do not affect the diffraction sub-profiles, (ii) if, however, $h + k+ l \neq 3$m, the diffraction sub-profiles broaden and/or are shifted. In a recent work a systematic numerical procedure has been developed to evaluate the density of planar defects together with dislocations and crystallite (or subgrain) size in *fcc* crystals [9]. Powder diffraction patterns have been calculated numerically by using the DIFFaX software [60] for intrinsic and extrinsic stacking faults, and twin boundaries for the first 15 Bragg reflections up to 20% fault density. A typical profile of the {422} Bragg reflection corresponding to 10% intrinsic stacking faults together with the constituting sub-profiles is shown in Fig. 11. It can be seen that, depending on the particular *hkl* values the sub-profiles are broadened and shifted to different extent. In [9] it was found that the Bragg reflections consist of five sub-reflection types, which can be categorized by specific selection rules for the *hkl* indices in accordance with the theory of Warren. The FWHM and the positions of some 15,000 sub-reflections have been parameterized in a concise manner and incorporated into the CMWP method. The eCMWP method, extended to evaluate planar defects was applied to determine the twin density in inert gas condensed and severely deformed copper and Cu–Zn alloys, respectively [9, 61]. It was found that in pure copper twinning becomes an essential alternative to dislocation activity when the grain size becomes smaller than about 40 nm, in good correlation with [57–59, 62, 63]. In HPT deformed Cu–Zn alloys twinning was observed to increase with plastic deformation [61], in agreement with TEM observations [64].

Conclusions

It is shown that X-ray line profile analysis is a powerful tool to characterize the microstructure of nanocrystalline materials in terms of (i) grain size, (ii) subgrain size, (iii) size distributions, (iv) dislocation densities, (v) dislocation character and arrangement, and (vi) stacking faults and twin boundaries. A systematic analysis of TEM and X-ray crystallite size shows that the X-ray size, especially in the case of nanostructural materials produced by plastic deformation, provides the average subgrain size and size distribution. The X-ray method is unlimited for the determination of dislocation densities in the upper dislocation density region. The thermal stability of nanostructural materials can be well determined by the X-ray method. It has been shown that in Ti the dislocation density decreases gradually with temperature, whereas the average crystallite size remains stable up to the recrystallization temperature. A systematic analysis has shown that stacking faults and twinning causes a different anisotropy in line broadening versus the *hkl* indices as compared to dislocations, which enables the determination of the densities of planar defect and dislocations at the same time.

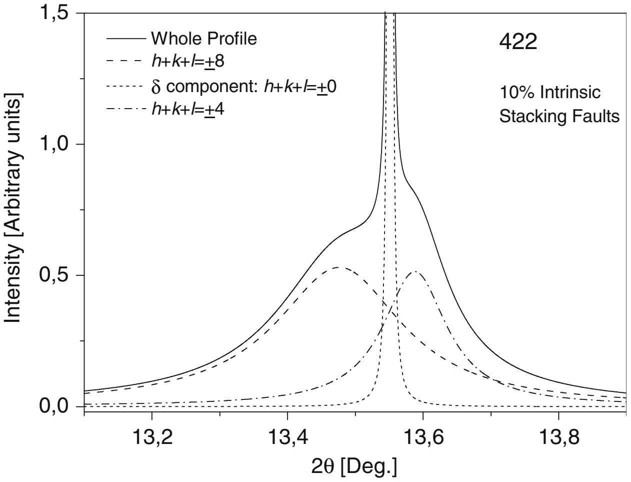

Fig. 11 Typical profile of the {422} Bragg reflection corresponding to 10% intrinsic stacking faults together with the constituting sub-profiles. The sub-profiles are broadened and shifted to different extent and in different directions, depending on the particular *hkl* values [9]. The uneffected, δ like function has the shape of the "instrumental profile" built into the DIFFaX software, cf. [60]

Acknowledgements The author is grateful to the Hungarian National Science Foundation, OTKA T46990 and OTKA T43247, for supporting this work.

References

1. Hellmig RJ, Baik SC, Bowen JR, Estrin Y, Juul Jensen D, Kim HS, Seo MH, December 2003, In: Zehetbauer MJ, Valiev RZ (eds) Proc. 2nd Int. Conf. Nanomater. Severe Plastic Deformation: Fundamentals – Processing – Applications, Wien, Austria, J.Wiley VCH, Weinheim, 2004 p 420
2. Scherrer P (1918) Göttinger Nachrichten 2:98
3. Warren BE, Averbach BL (1950) J Appl Phys 21:595
4. Warren BE, Averbach BL (1952) J Appl Phys 23:497
5. Warren BE (1959) Prog Metal Phys 8:147
6. Wilson AJC (1962) In: X-Ray Optics; the Diffraction of X-Rays by Finite and Imperfect Crystals, Methuen, London
7. Bertaut EF (1950) Acta Cryst 3:14
8. Wilkens M Fundamental Aspects of Dislocation Theory, edited by J.A Simmons, R de Wit, R Bullough, Vol. II Nat Bur Stand (US) Spec. Publ. No. 317, Washington, DC. USA, 970 p 1195
9. Balogh L, Ribárik G, Ungár T (2006) J Appl Phys 100:023512
10. Krill CE, Birringer R (1998) Phil Mag A 77:621
11. Langford JI Louër D (1996) Rep Prog Phys 59:131
12. Ungár T, Borbély A, Goren-Muginstein G R, Bergerand S, Rosen A R (1999) Nanostructured Mater 11:103
13. Langford JI, Louër D, Scardi P (2000) J Appl Cryst 33:964
14. Valiev RZ, Kozlov EV, Ivanov Yu F, Lian J, Nazarov AA, Baudelet B (1994) Acta Met Mater 42:2467
15. Terwilliger ChD, Chiang YM (1995) Acta Met Mater 43:319
16. Scardi P, Leoni M (2002) Acta Cryst A58:190
17. Hinds WC In: Aerosol technology. Properties, behavior and measurement of airbone particles, (Wiley, New York, 1982)
18. Ribárik G, Ungár T, Gubicza J (2001) J Appl Cryst 34:669
19. Ungár T, Gubicza J, Ribárik G, Borbély A (2001) J Appl Cryst 34:298
20. Ribárik G, Gubicza J, Ungár T (2004) Mat Sci Eng A387–389:343
21. Ungár T, Borbély A (1996) Appl Phys Lett 69:3173
22. Ungár T, Tichy G (1999) Phys Stat Sol (a) 171:425
23. Ungár T, Ott S, Sanders PG, Borbély A, Weertman JR (1998) Acta Mater 46:3693
24. Mitra R, Ungár T, Morita T, Sanders PG, Weertman JR (1999) In: Chung YW, Dunand DC, Liaw PF and Olson GB (eds) Advanced Materials for the 21st Century, Warrendale TMS, USA, p 553
25. Mitra R, Ungár T, Weertman JR (2005) Trans Indian Inst Metals 58:1125–1132
26. Gubicza J, Balogh L, Hellmig RJ, Estrin Y, Ungár (2005) T Mat Sci Eng A 400–401:334–338
27. Sanders PG (1996) Ph.D. Thesis, Northwestern University, Evanston, IL, USA 60208
28. Zhilyaev AP, Gubicza J, Nurislamova G, Révész Á, Suriñach S, Baró MD, Ungár T (2003) Phys Stat Sol (a) 198:263

29. Gubicza J, Chinh NQ, Horita Z, Langdon TG (2004) Mater Sci Eng A 387–389:55
30. Zhu YT, Huang JY, Gubicza J, Ungár T, Wang YM, Ma E, Valiev RZ (2003) J Mat Res 18:1908
31. Bolmaro RE, Brokmeier HG, Signorelli JW, Fourtz A, Bertinetti MA (2004) In: Mittemeijer EJ, Scardi P (eds) Diffraction analysis of the microstructure of materials, Springer, Berlin, p 391
32. Ungár T, Tichy G, Gubicza J, Hellmig RJ (2005) J Powder Diffraction, 20:366
33. Krivoglaz M A theory of X-ray and thermal neutron scattering by real crystals Berlin: Springer-Verlag; 1996
34. Groma I (1998) Phys Rev B 57:7535
35. Klimanek P, Kuzel R Jr (1988) J Appl Cryst 21:9
36. Kuzel R Jr, Klimanek P (1988) J Appl Cryst 21:363
37. Kuzel R Jr, Klimanek P (1989) J Appl Cryst 22:299
38. Thiele E, Klemm R, Hollang L, Holste C, Schell N, Natter H, Hempelmann R (2005) Mat Sci Eng A 390:42
39. Caglioti G, Paoletti A, Ricci FP (1958) Nucl Instrum 3:223
40. Ungár T, Gubicza J, Tichy G, Pantea C, Zerda TW (2005) Composites:Part A 36:431
41. Wilkens M (1970) Phys Stat Sol (a) 2:359
42. Stokes AR, Wilson AJC (1944) Proc Cambridge Phys Soc 40:197
43. Stephens PW (1999) J Appl Cryst 32:281
44. Steeds JW (1973) In introduction to the anisotropic elasticity theory of dislocations. Oxford, Clarendon
45. Popa NC (1998) J Appl Cryst 31:176
46. Dragomir IC, Ungár T (2002) J Appl Cryst 35:556
47. Ungár T, Dragomir I, Révész Á, Borbély A (1999) J Appl Cryst 32:992
48. Dragomir IC, Ungár T (2002) Powder Diffr 17:104
49. Cordier P, Ungár T, Zsoldos L, Tichy G (2004) Nature 428:837
50. Nyilas K, Dupas C, Kruml T, Zsoldos L, Ungár T, Martin JL (2004) Mat Sci Eng A 387:25
51. Gubicza J, Kassem M, Ribárik G, Ungár T (2004) Mat Sci Eng A 372:115
52. Fátay D, Bastarash E, Nyilas K, Dobatkin S, Gubicza J, Ungár T (2003) Metallkd Z 94:7
53. Balogh L, Gubicza J, Hellmig RJ, Estrin Y, Ungár T (2006) Z Kristallography 23:381
54. Gubicza J, Nam NH, Balogh L, Hellmig RJ, Stolyarov VV, Estrin Y, Ungár T (2004) J Alloy Compd 378:248
55. Wang YM, Chen MW, Zhou FH, Ma E (2002) Nature 479:912
56. Kuzel R, Cernansky M, Holy V, Kubena J, Simek D, Kub J (2004) In: Mittemeijer EJ, Scardi P (eds) Diffraction analysis of the microstructure of materials, Springer, Berlin, p 229
57. Meyers MA, Vöhringer O, Lubarda VA (2001) Acta Mater 49:4025
58. Dragomir IC, Ungár T, Chen M, Ma E, Hemker KJ, Sheng H, Wang YM, Cheng X (2003) Science 300:1275
59. Liao XZ, Huang JY, Zhu YT, Zhou F, Lavernia E (2003) J Philos Mag 83:3065
60. Treacy MMJ, Newsam JM, Deem MW (1991) Proc Roy Soc London A 433:499
61. Ungár T, Balogh L, Zhu Y T, Horita Z, Xu C, Langdon TG (2006) submitted to Mater Sci Eng A
62. Zhu YT, Liao XZ, Srinivasan SG, Zhao YH, Baskes MI, Zhou F, Lavernia E (2004) J Appl Phys Lett 85:5049
63. Zhu YT, Liao XZ, Srinivasan SG, Lavernia EJ (2005) J Appl Pys 98:034319/1–8
64. Zhao YH, Liao XZ, Zhu YT, Horita Z, Langdon TG (2005) Mater Sci Eng A410–411:188